Design and Dynamic Analysis of a Spanwise Morphing Wing for Mars Exploration

Guanzhen Wu , Yaohua Tong , Jiaying Zhang , Zhen Zhao

PII: S1270-9638(24)00715-6
DOI: https://doi.org/10.1016/j.ast.2024.109586
Reference: AESCTE 109586

To appear in: *Aerospace Science and Technology*

Received date: 23 June 2024
Revised date: 3 August 2024
Accepted date: 9 September 2024

Please cite this article as: Guanzhen Wu , Yaohua Tong , Jiaying Zhang , Zhen Zhao , Design and Dynamic Analysis of a Spanwise Morphing Wing for Mars Exploration, *Aerospace Science and Technology* (2024), doi: https://doi.org/10.1016/j.ast.2024.109586

Highlights

- Introduces a modular variable spanwise morphing wing for high-aspect-ratio aircrafts, which is possible to transport and launch large-size Mars exploration UAVs
- A rigid origami skin is proposed, which maintains the airfoil's continuous smoothness after spanwise morphing.
- A lockable structure is designed, and the main factors affecting the self-locking property are analysed.
- The kinematics of the spanwise morphing wing unit is developed to study fully expanded time.
- Fluid-structure interaction analysis is performed to investigate the spanwise morphing mechanism and origami skin response under aerodynamic loads.

Design and Dynamic Analysis of a Spanwise Morphing Wing for Mars Exploration

Guanzhen Wu, Yaohua Tong, Jiaying Zhang*and Zhen Zhao

[1]School of Aeronautic Science and Engineering, Beihang University, Beijing 100191, China

*Corresponding author: E-mail: jiaying.zhang@buaa.edu.cn

Abstract

The application of spanwise morphing wings makes it possible to transport and launch large-size Mars exploration UAVs. This article proposes a modular variable spanwise morphing wing for high-aspect-ratio aircrafts, and analyses the characteristics of the morphing wing by theoretical analysis, numerical simulation and experimental verification. The novel spanwise morphing wing is based on the Sarrus-inspired deployable structure, which can increase the wing's lift by changing the spanwise length. The pre-strain torsion springs are assembled to provide the initial driving moment of the morphing mechanism. A regular triangle cross section is selected by evaluating the bending and torsional stiffness, and deployable triangular prism mechanisms are identified. Through releasing the pre-strain torsion springs to achieve expansion and implant Sarrus linkages along the straight motion paths. A lockable structure is designed, and the main factors affecting the self-locking property are analysed. A rigid origami skin is proposed, which maintains the airfoil's continuous smoothness after spanwise morphing. The kinematics of the spanwise morphing wing unit is developed using the Lagrange equation, and the theoretical models of morphing wings with different numbers of units are obtained. The unit numbers influence fully expanded time, and the time decreases gradually along the wingtip's direction. Finally, a one-way fluid-structure interaction analysis is performed to investigate the spanwise morphing mechanism and origami skin response under aerodynamic loads. Results show that the skeleton mechanism's maximum stress is below the material's yield strength, and the origami skin's maximum out-of-plane deformation is less than 0.5% of the wing chord, which provides a necessary theoretical basis for applying the spanwise morphing wing.

Keywords

Mars exploration, spanwise morphing wing, origami skin, dynamic, fluid-structure coupling

1. Introduction

Exploring terrestrial planets such as Mars involves the use of orbiters, landers, and rovers. Cameras on orbiters created a global Mars map at a resolution ratio of about 0.3 meters per pixel. Other vehicles can carry more instruments to depict smaller local areas at a higher map resolution [1], such as Perseverance. However, numerous areas of Mars remain uncharted except for images from orbiters, and current instruments cannot probe temperatures within several kilometres of the Martian surface. A large-size aircraft would fill such a research gap [2].

Previously, several vehicles were proposed for near-surface Mars exploration. Most of these concepts were based on powered flying vehicles, including chemical or electric propulsion, which would produce enormous penalties on the aircraft's mass and complexity [3]. The concepts of helicopters and sailplanes for Mars exploration will significantly help future discoveries. In 2020, a small helicopter was designed by NASA Jet Propulsion Laboratory (NASA JPL) and took off with the Mars Perseverance Rover [4]. It made the first flight on the Martian surface, but each flight lasted only about two minutes. NASA Langley proposed an autonomous aircraft, the Aerial Regional-scale Environmental Survey (ARES), as a discovery mission candidate [5]. The aircraft was originally planned to conduct a one-hour atmospheric exploration mission, but it was unsuccessful due to insufficient atmospheric data. An alternative approach is the use of an unpowered sailplane. The Prandtl-m is a sailplane based on the high-aspect-ratio wing concept. However, the sailplane can only fly for about 10 minutes. Zdravko Terze et al. [6] proposed a new optimization algorithm for developing an insect-type vehicle that flies in the Martian atmosphere, and the optimization process utilized the flapping pattern optimization method based on the quasi-steady aerodynamic model. Adrien Bouskela et al. [7] designed a sailplane for Mars exploration, which took dynamic flying by the

atmospheric wind gradients and static flying by slope or thermal updrafts. These flight concepts would effectively alleviate the energy and weight constraints associated with traditional powered flight, thereby offering significant advancements in aviation technology.

Among the limitations of previous Mars exploration aircrafts, the most pivotal is the short flight time. To overcome this disadvantage, a vehicle with a high-aspect-ratio wing is significant. However, the limited space of launch vehicles restricts the transportation of high-aspect-ratio aircraft. Consequently, the spanwise morphing wing concept makes up for the deficiency in this limitation.

A large wingspan improves aerodynamic efficiency but reduces manoeuvrability compared to a small wingspan [8]. The spanwise morphing technology enables the integration of the benefits associated with both high-aspect-ratio and low-aspect-ratio wingspans in a single aircraft, thereby effectively facilitating the accomplishment of various flight tasks. Ajaj et al. [9] studied the advantages of variable spanwise morphing wings to improve aerodynamic and roll control efficiency when expanded asymmetrically. Weisshaar designed a telescopic wing and achieved a spanwise extension of up to 60% by using the pneumatic actuator [10]. Zhang et al. [11] analysed the buckling behaviour of the composite morphing wing. They discovered that under the control of aerodynamic loads, the spanwise torsion deformation could improve the distribution of the aerodynamic load. Sadique et al. [12] proposed a variable wing concept that could realize chord and camber morphing. The flight performance showed higher aerodynamic efficiency of the morphing wing than the traditional wing at different AOA. Lockheed Martin designed a folding wing to achieve spanwise variation and increase the flight performance of the aircraft [13].

Recently, many spanwise morphing wing concepts have been designed, from the inflatable wing [14,15] to the pneumatic telescopic wing [16] and the servo-actuated telescopic wing [17]. Samuel et al. [18] proposed a telescopic wing concept in which a hollow shell was used to maintain the aerofoil shape, and they utilized inflatable actuators to withstand aerodynamic loads. Ajaj et al. [19] utilized the mechanism with rack and pinion to achieve both symmetric and asymmetric spanwise extension of a spanwise morphing UAV. Michael et al. [20] designed a non-elastic morphing wing skin and analyzed the in-plane deformability and out-of-plane stiffness of the morphing wing

skin. Ajaj et al. [21] carried out a Zigzag wing box, which allowed for a 44% variation in wingspan. This concept was incorporated into a morphing UAV to verify its flight characteristics and roll control capacity. Several investigations have been conducted to analyse the dynamic characteristics of morphing wings. Snyder et al. [22] utilized the FE approach to investigate the natural frequency of a foldable wing. Zhang et al. presented a new concept that used a designed negative stiffness to generate resonance passive energy balance on deformed blades, reducing the structural natural frequency to the required driving frequency [23]. They implemented a passive energy balancing concept into a morphing wingtip and established the kinematics of the negative stiffness system [24]. Pulok et al. [25] discussed the vibration characteristics of a morphing wing and concluded that the natural frequency decreases when the spanwise length of the wing is increased. Yang et al. [26] designed a modular skeleton mechanism of a morphing wing utilizing the bilateral triangular pyramid, which can perform the variable spanwise twist, sweep, and bend. The FSI analysis of the morphing wing showed that the flexible skin's out-of-plane expansion deformation at the leading edge contributed to the improved aerodynamic characteristics. Gamboa et al. [27] analysed the modal characteristics of a composite spanwise morphing wing to obtain free vibration's natural frequency and mode shapes. Bae [28] proposed the aerodynamic analysis of a span morphing wing on a cruise missile, and then Neal [29] built a model with 7 DOF of this wing concept. Zhang et al. [30] developed a camber-morphing-wing's low-fidelity model and utilized the chord-wise dimension and flexibility to obtain the potential critical speed.

Several flexible structures [31] and foldable mechanisms [32,33]were developed to overcome the limitations of deformation ability and improve the stiffness of the morphing structure. Amoozgar investigated the effects of different dimensions of the cross-section of a rotor blade on the efficacy of the torsional deformation concept and developed a cross-section consistent with a coupling of low extension-twist and high lag-twist [34]. Jenett [35] designed a modular wing that used light-weight and high-strength carbon fibre cells to achieve continuous spanwise twist morphing. The modular wing performed higher roll efficiency compared with the traditional wing with a rigid aileron system. Mahid introduced a novel flexible fairing design to avoid the gaps on the aerodynamic surface and reduce the fairing's rotational stiffness and the pressure on the surface while maintaining the smoothness of the aerodynamic surface [36].

The concept of a Mars exploration mission of the proposed morphing aircraft is shown in Figure 1. The assumption is made that a spacecraft is launched from Earth and directed onto a trajectory to Mars lasting 7 months. The rocket gets entry into the Martian atmosphere by utilizing the interplanetary orbit with a series of trajectory correction manoeuvres (TCMs) [5]. Then the spanwise morphing UAV will separate from the carrier space vehicle. At the same time, the morphing wing segment will deploy immediately and achieve a rigidized shape. Finally, the aircraft can conduct scientific exploration using two flight strategies: dynamic soaring utilizing the wing gradients and static soaring utilizing slope or thermal updrafts [7].

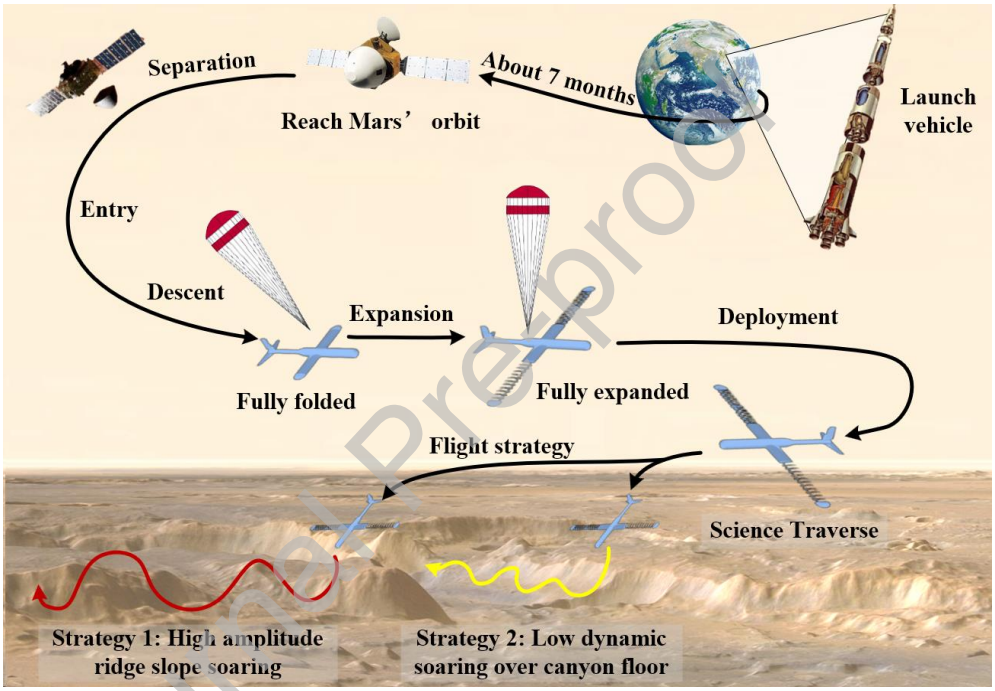

Figure 1. Mars exploration mission concept overview.

This article proposes a spanwise morphing wing with a foldable truss structure and the origami skin. Each foldable truss unit is composed of six rotating rods, with torsion springs strategically positioned at the joint between the wing rib and the rotating rod to provide the initial driving moment for the morphing mechanism. The lockable structure and the Miura-Waterbomb origami skin are designed to achieve the spanwise morphing function. The rest of this article is structured as follows. Section 1 presents the structure and composition of the spanwise morphing wing, and structural dimensions and configuration parameters of different components are discussed. Section 2 constructs the dynamic theoretical models of spanwise morphing wings with varying numbers of units. Section 3 conducts the one-way FSI analysis on the spanwise morphing wing unit. Section

4 introduces a flight test of the spanwise morphing UAV. Conclusions are drawn in Section 5.

2. Design of the spanwise morphing wing

2.1. Structure and composition of the wing

The novel spanwise morphing mechanism concept is based on the Sarrus linkage [37]. The original Sarrus linkage design for the spanwise morphing wing is shown in Figure 2 (a). The solid line represents a certain instantaneous position of the Sarrus linkage mechanism during the deformation process, and the dashed line is the position when the deformation is completed. Figure 2 (b) displays the prototype of the Sarrus linkage mechanism attached to an aircraft wing. The Sarrus linkage belongs to an over-constrained connection type, which is an SDOF mechanism. Therefore, the Sarrus linkage mechanism usually requires only one actuator to drive a root link, thereby driving the whole linkage mechanism to achieve the deformation along the spanwise direction.

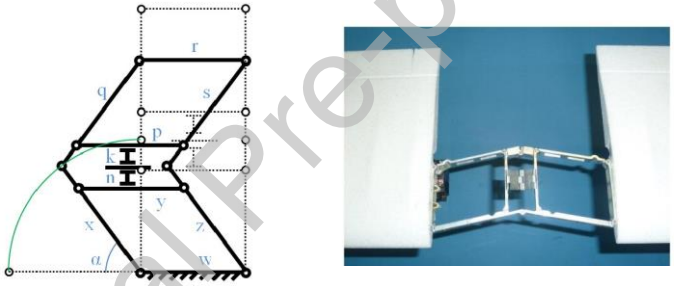

(a) (b)

Figure 2. Concept of the Sarrus linkage mechanism: (a) the schematic of the morphing mechanism; (b) the prototype of the mechanism attached to a wing [37].

The spanwise morphing mechanism design consists of three double-link units connected by rotating joints, as shown in Figure 3.

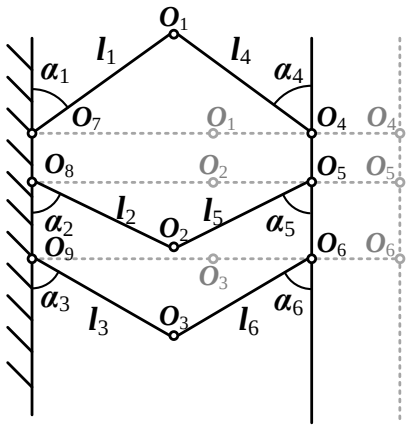

Figure 3. Concept of the spanwise morphing wing mechanism.

In this mechanism, the links l_1, l_2, l_3, l_4, l_5, l_6 have the same length,

$$l_1 = l_2 = l_3 = l_4 = l_5 = l_6 = l \quad (1)$$

Meanwhile,

$$\alpha_1 = \alpha_2 = \alpha_3 = \alpha_4 = \alpha_5 = \alpha_6 = \alpha \quad (2)$$

where α_i is the rotation angle of link l_i. The links l_1 and l_4 are connected by revolute joint O_1. The other ends of links l_1 and l_4 are connected to the boundary by O_4 and O_7. The revolute joints O_4 and O_7 only move horizontally, so this mechanism is SDOF.

The spanwise morphing wing is developed based on this linkage, as shown in Figure 4 (b). d_1, d_2, d_3, d_4, d_5, d_6 are rotating rods, and R_1, R_2, R_3, R_4, R_5, R_6, R_7, R_8, R_9 are rotating joints. The length of rotating rods and the rotating angle of joints are the same as those in the Sarrus linkage shown in Figure 3.

Figure 4 (a) shows that the wing of the Mars exploration vehicle contains two parts: a fixed-wing segment near the root and a morphing wing segment near the tip. Once the vehicle is separated from the carrier spacecraft after entering the Martian atmosphere, the dragrope will be released, and the morphing wing segment will deploy immediately and achieve a rigidized shape. Each end of the dragrope is connected to two adjacent wing ribs. The morphing wing segment is composed of multiple modular spanwise morphing wing units. Each unit has two rigid ribs, six rotating rods, six torsion springs, and one origami skin, as shown in Figure 4 (c). The rotating rods and the wing ribs are hinged through the rotating joints to form a spanwise morphing unit, and the rotating joints between the rotating rod and the rigid rib are established through the interference assembly between the bearing and the axle, as shown in Figure 4 (d) and Figure 4 (e).

The lockable structure is shown in Figure 4 (f), which can improve the stiffness and stability of the wing structure after morphing. It is a snap-fit structure with two main elements: the deflection element fixed on the wing rib and the retaining element fixed on the rotating rod. During the self-locking process, the deflection element will be elastically morphed and returned to the original position after the self-locking process is completed. Therefore, the rotating rod will be locked, and the spanwise morphing unit will be transformed into a stable structure.

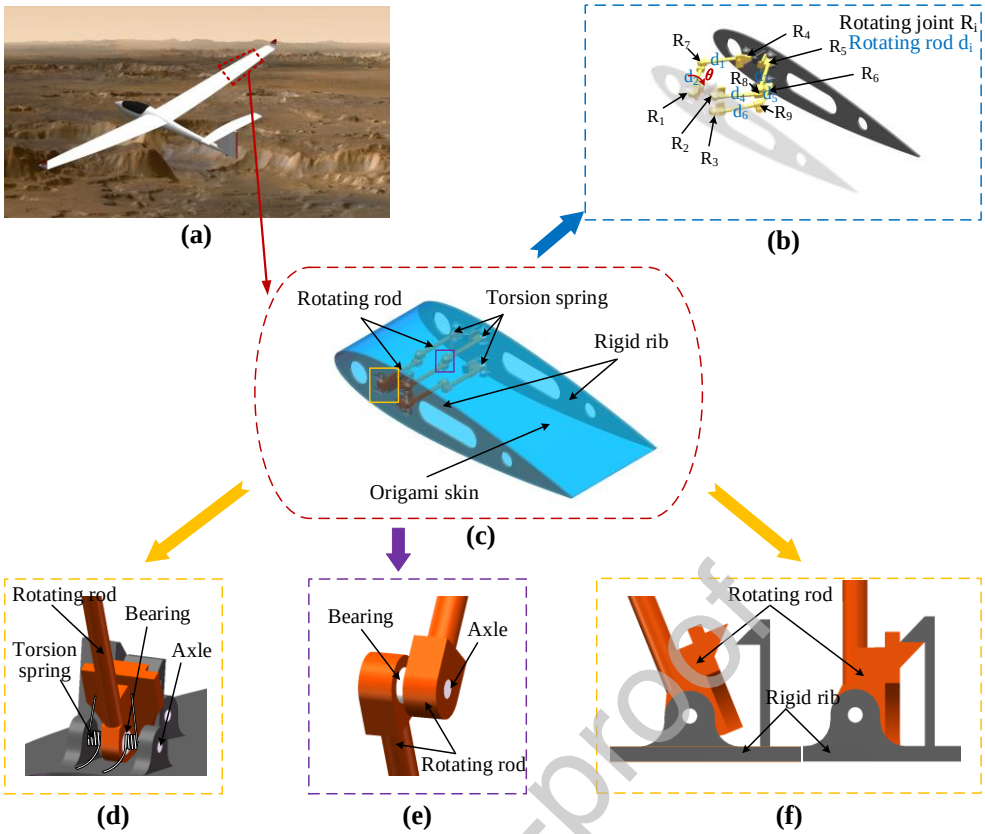

Figure 4. Composition of the spanwise morphing wing: (a) the Mars exploration vehicle with spanwise morphing wing; (b) the morphing schematic diagram; (c) the spanwise morphing wing unit; (d) connection between the rotating rod and wing rib; (e) connection between two rotating rods; (f) the lockable structure.

The process of a spanwise morphing wing with five units from fully folded to fully expanded is shown in Figure 5. For each unit, when it fully folds, the rib spacing is 66mm, and it's 144mm when the unit fully expands. In other words, the maximum spanwise changing ratio for the morphing wing is 118.18%, more significant than 100%.

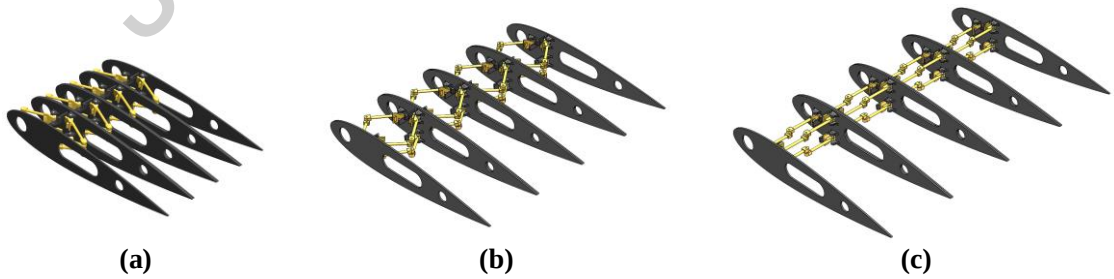

Figure 5. The spanwise morphing process: (a) fully folded; (b) half expansion; (c) full expansion.

The design of the spanwise morphing wing focuses on matching wing rib sizes and determining the origami skin scheme to assemble a complete wing unit. The wing

mechanism is solely operated by torsion springs, without the need for additional actuators. Additionally, the rotating rods achieve a spanwise morphing function and raise the structural stiffness, which replaces the conventional wing beam and significantly reduces the morphing wing's structural mass. Besides, the modular design and distributed drive of torsion springs can achieve the rapid deformation of the spanwise morphing wing, significantly reducing the demand for the local driving force.

2.2. Configuration of the rotating rods

A foldable truss structure comprises several rotating rods, which are adapted to replace the beam structure of the traditional single-beam wing. Since there are many options for the cross-section shape of the foldable truss along the wing chord, the comparison and selection of the cross-section shape will be necessary. The regular triangle, quadrilateral, hexagon and octagon are selected (if the cross-section polygon has a more significant number of sides, the complexity of the morphing mechanism will increase dramatically, so it is not within the scope of this scheme). It is assumed that the polygons are all regular, and the torsional stiffness and bending stiffness for the *y*-axis and *z*-axis that are over-centroid and perpendicular to each other are considered, as shown in Figure 6.

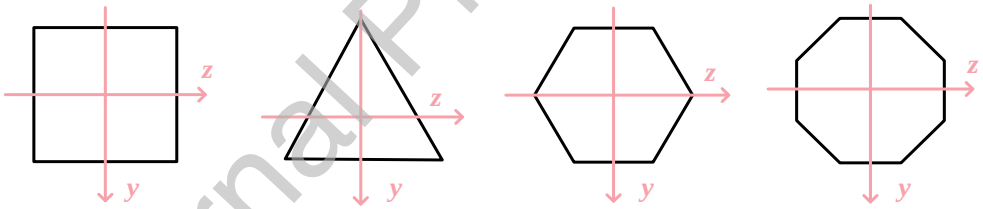

Figure 6. Cross-section shapes with different numbers of sides: (a) quadrilateral; (b) triangle; (c) hexagon; (d) octagon

Taking the regular triangle as an example, its torsional stiffness and bending stiffness can be respectively defined by its polar moment of inertia and moment of inertia, which can be described as

$$\mathrm{I}_p = \frac{\sqrt{3}a^4}{80} = 0.115A^2 \tag{3}$$

$$\mathrm{I}_z = \frac{\sqrt{3}a^4}{96} = 0.096A^2 \tag{4}$$

where I_p is the polar moment of inertia, I_z is the moment of inertia, a is the length of the side and A is the area of the triangle.

Considering the influence of each additional edge of the cross-section shape on the total structural mass, the mass normalization is calculated and the results are shown in Figure 7. The triangular shape has higher torsional and bending stiffness to ensure the light weight of the structure, therefore the triangular shape is selected as the cross-section shape of the foldable truss.

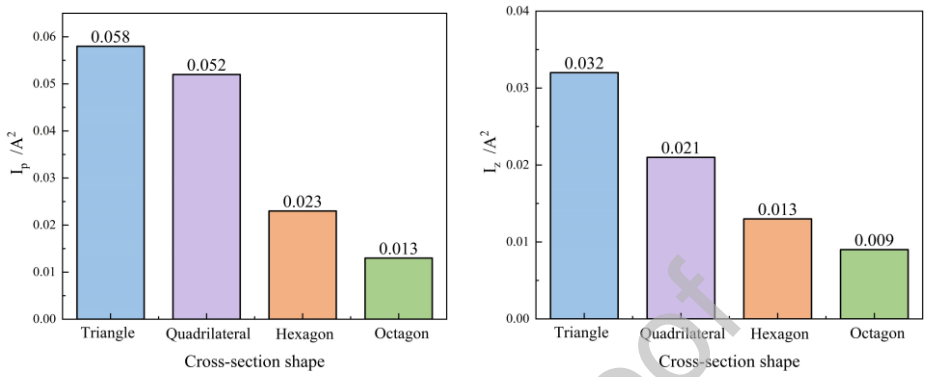

(a) **(b)**

Figure 7. The polar moment of inertia and moment of inertia of different cross-section shapes after quality normalization.

Meanwhile, the position and dimensions of the triangular shape also greatly influence the stiffness and mass of the morphing structure. To get a better bearing capacity, the centroid of the triangular section is selected at the aerodynamic focus of the airfoil (the position of 25% chord length). The rotational axis formula of the moment of inertia is used to decide the position and dimensions of the triangle, which can be described as

$$I_v = \frac{I_y+I_z}{2} - \frac{I_y-I_z}{2}\cos 2\alpha + I_{yz}\sin 2\alpha \quad (5)$$

where $I_z = \frac{bh^3}{36}, I_y = \frac{bh^3}{12}, I_{yz} = 0, b$ and h are the length of the base and height of the triangle, α is the rotation angle of the v-axis, as shown in Figure 8.

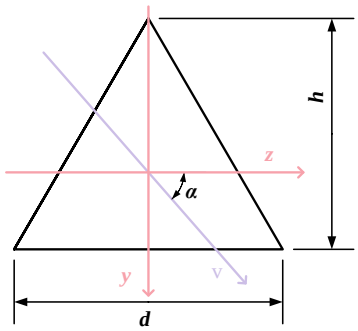

Figure 8. The position and dimensions of the triangle.

Therefore, the bending stiffness of the triangle relative to the v-axis can be expressed as

$$I_v = \frac{bh^3}{18} - \frac{bh^3}{36}\cos 2\alpha \quad (6)$$

where $0° \leq \alpha \leq 90°$.

It can be observed that the I_v will obtain the maximum when $\alpha = 90°$. Meanwhile, considering the size limitations of the airfoil, the dimensions are finally chosen as $d =$ 34mm and $h = 45$mm.

2.3. Design and analysis of the lockable structure

Figure 9 (a) shows that one lockable structure is composed of a deflection element fixed on the wing rib and a retaining element fixed on the rotating rod, which can be simplified into a snap-fit and a rigid body with a fixed axis of rotation, as shown in Figure 9 (b). During the assembly process, the snap-fit requires flexibility in its moving direction to achieve elastic deflection. Therefore, the assembly Moment (M) is supposed to be greater than the characteristic moment M_{min} (minimum driving moment), ensuring that the deformation process can be completed.

It is assumed that the retaining element fixed on the rotating rod is a rigid body. Three dimensions that significantly influence the self-locking property are shown in Figure 9 (b), where L is the beam's length, Y is the beam's depth, and α is the slope surface's angle.

The relationship between the energy absorption (E) and the snap-fit assembly moment (M) during the assembling process is simulated in ABAQUS, as shown in Figure 9 (c). The assembly moment and rotation angle of the rigid body are obtained in the simulation, and the energy absorption is calculated from the area enclosed by the Moment-Angle curve and the X-axis.

It shows that the beam's length (L) has a great influence on the snap-fit property. Meanwhile, it determines the structural size and available space for the morphing mechanism. As shown in Figure 9 (d) and Figure 9 (g), when the length of $L < 15.5$mm, the maximum assembly moment and the maximum energy absorption are 20 Nmm and 1.7 mJ. That indicates the beam with a shorter length needs the larger assembly moment to achieve the same deflection, which may cause structural damage during assembly. However, if the length of L is too large, more span space of the wing will be taken up and the elongation will be reduced. Therefore, it is necessary to choose a reasonable beam length.

The depth (Y) determines the maximum deflection of the snap-fit during the assembly process. As shown in Figure 9 (e) and Figure 9 (h), the assembly moment and energy absorption continuously increase with the increase of Y. If Y is too small, the self-locking performance of the snap-fit will be significantly reduced. On the other hand, if Y is too large, the structure may be damaged.

The angle of the insertion face (α) also affects the assembly moment and energy absorption of the snap-fit structure. As shown in Figure 9 (f) and Figure 9 (i), the required assembly moment (M) increases with the increase of the angle of the slope surface (α). That's because the angle of the slope surface and the bending deflection of the beam continuously increase during the assembly process. Therefore, a reasonable value of α is necessary to reduce damage to the beam structure when α is too large and avoid loss of self-lock performance when α is too small. The insertion face angle is selected to be between 40° and 50°.

Finally, in order to find out a smaller energy absorption value as well as a smaller bending moment, the dimensions of the snap-fit are chosen as $L = 16.5\text{mm}, Y = 3.5\text{mm}$ and $\alpha = 45^\circ$.

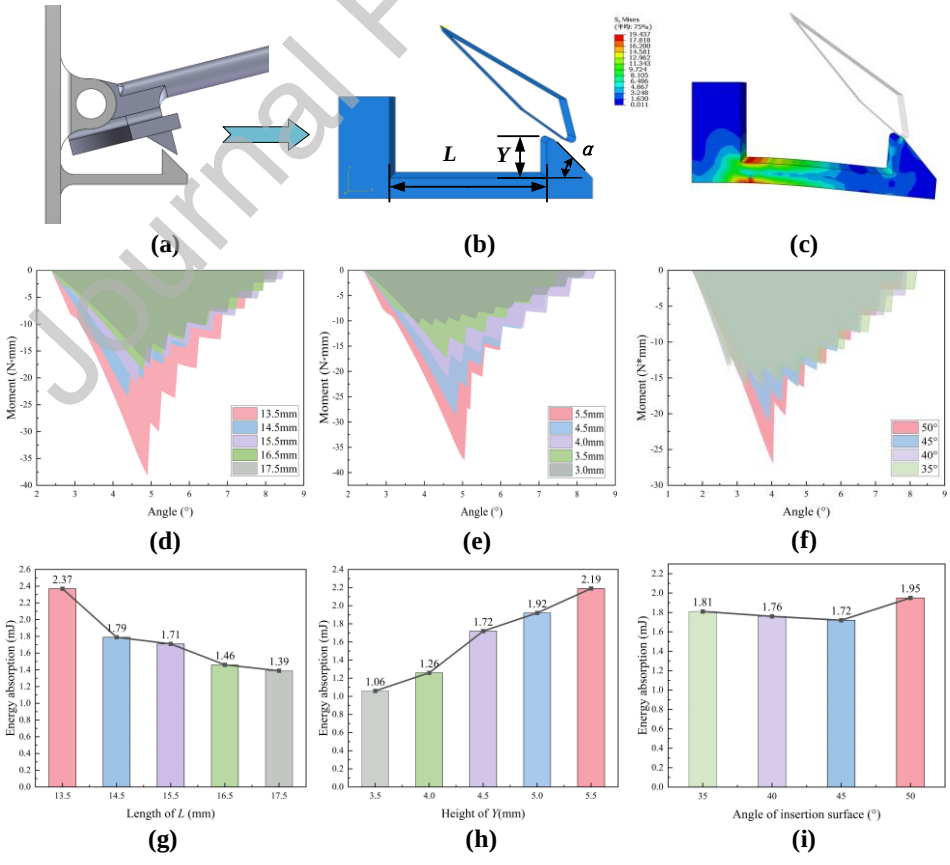

Figure 9. Main factors affecting the mechanical properties of the lockable structure: (a) a 3D model; (b) the FE model; (c) the stress distribution during the assembly process; (d)(g) Moment-Angle curves and the energy absorption with different beam length(L); (e)(h) Moment-Angle curves and the energy absorption with different depth(Y); (f)(i) Moment-Angle curves and the energy absorption with different insertion face angles(α).

2.4. Design of the origami skin

Combining the crease and folding characteristics of the Miura origami and the Waterbomb origami, a Miura-Waterbomb origami skin is proposed in this article. As shown in Figure 10, the airfoil curve is split into several polylines with end-to-end meetings. The length of each polyline is L_i, and the angle between the two adjacent polylines is θ_i. Taking the first two polylines as an example, the skin can achieve rigid folding along the shown creases in Figure 10, where the solid line represents the mountain crease and the dotted line represents the valley crease.

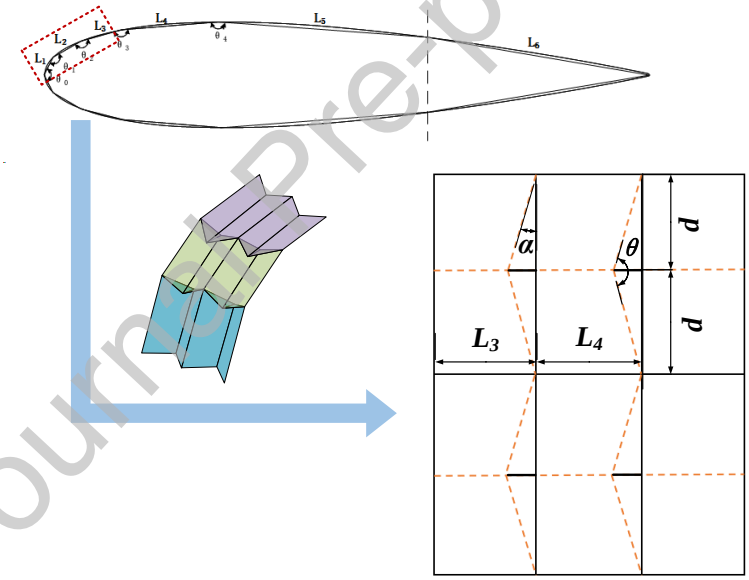

Figure 10. Principle of the origami skin design.

Figure 11 represents the side view when the skin is folded only along the horizontal crease and when fully folded along all creases, respectively. α is the angle between the inclined valley crease and the vertical mountain crease, θ is the angle between the two adjacent inclined valley creases, and β_1 and β_2 are the residual angle of α in different rectangles. Therefore, $\alpha + \beta_1 = \frac{\pi}{2}$, $\alpha + \beta_2 = \frac{\pi}{2}$ and $\beta_1 + \beta_2 = \theta$. As a result, the geometric conditions for rigid folding of the Miura-Waterbomb origami skin can be expressed as

$$L_1 = L_3,\ L_2 = L_4, \theta = \pi - 2\alpha \quad (7)$$

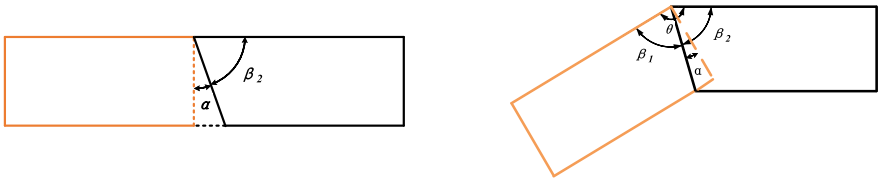

(a) **(b)**

Figure 11. Schematic diagram to prove the rigid folding geometry conditions.

The final design of the Miura-Waterbomb origami skin is shown in Figure 12. One edge of the skin is laid from the trailing edge, passing through the leading edge for a circle and reaching the trailing edge again to form a closure.

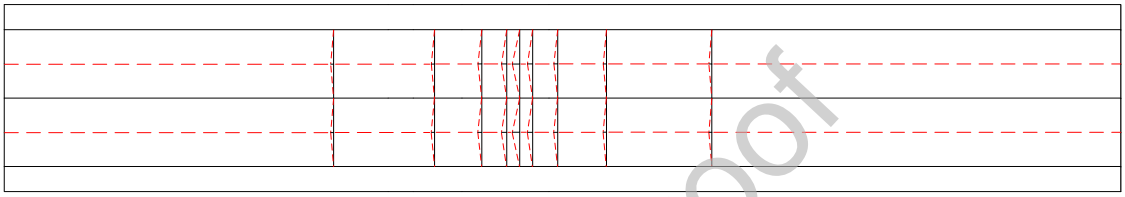

Figure 12. The final design of the Miura-Waterbomb origami skin.

2.5. Model assembly

The spanwise morphing wing unit model is produced by 3D printing, and the assembled model is shown in Figure 13. The ribs and rotating rods are made of PLA, and the skin is made of PET sheets with 0.2mm thickness. The laser cutting machine slots the grooving process of the creases, and the grooving depth is about half-thickness of PET sheets. The spanwise morphing process of the unit model is in line with expectations, and the skin's surface after morphing is continuous and smooth.

Figure 13. The spanwise morphing wing unit model.

Figure 14 shows the prototype of the spanwise morphing UAV and the planform of the morphing wing segment, which is equipped with a fixed-wing UAV flight platform. The

whole wing consists of the inner wing and the spanwise morphing wing. The origami skin is attached to the wing ribs of the spanwise morphing wing segment and the rigid skin is attached to wing ribs of the inner wing segment. A common wing rib connects the spanwise morphing wing segment and the inner wing segment. Detailed parameters of the aircraft with the spanwise morphing wing are listed in Table 1.

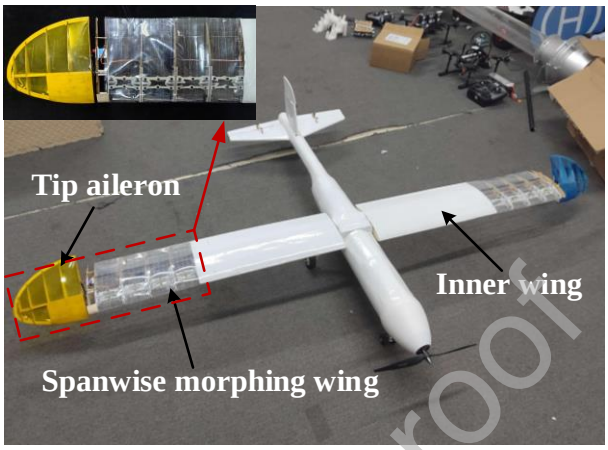

Figure 14. The fixed-wing UAV flight platform with spanwise morphing wing segment.

Table 1. Design parameters of the aircraft with the spanwise morphing wing.

Parameter	**Symbol**	**Value**
Total mass (kg)	m	3.01
Wingspan (m)	b	2.00
Wing area (m^2)	S	0.40
Wing chord (m)	c	0.20
Aspect ratio	AR	10
Fuselage length (m)	L_f	1.58

Table 2 lists the parameter comparison between the proposed novel spanwise morphing wing and other wings used for Mars exploration. Most of the existing designs for Mars exploration adopt the fixed wing scheme, which has a large wing span to provide enough lift for the Mars aircraft. However, the large size of fixed wings requires great demands on the transportation space of launch vehicle. Therefore, the spanwise morphing mechanism and lower cruising speed design make it possible for exploration aircrafts to transport and deploy on Mars.

Table 2. Parameter comparison between different wings used for Mars exploration.

Aircraft name	**Wing type**	**Wing span(m)**	**Aspect Ratio**	**Wing area(m^2)**	**Cruising speed(m/s)**

Novel aircraft	Stretchable	2.00	10.0	0.40	40.0
ARES airplane [5]	Fixed	6.25	5.0	7.00	145.0
Mars sailplane [7]	Fixed	3.35	6.2	1.80	70.0
Mars airplane [38]	Folded	2.60	5.4	1.25	6.0

3. Dynamic analysis of the spanwise morphing wing

3.1. Dynamic modeling of the spanwise morphing unit

The equivalent simplification of the spanwise morphing wing unit is established to ensure that the mechanical and dynamic models are consistent with the real ones, and most of the parts that have none or negligible influence on the calculation results are eliminated. Smooth hinges construct the rotating joints, and the torsion spring is settled at the root of the rotating rod. The torsion spring releases the elastic potential energy to drive the whole wing unit to spread. Since the DOF of a spanwise morphing wing unit is 1, each rotating rod's length and rotation angle are the same. Thus, the wing unit is equivalent to a planar multi-link mechanism, as shown in Figure 15 (a). Due to the small mass of the origami skin, its impact on the total kinetic energy of the system can be ignored. Only the influence brought by the elastic energy at the crease to the total potential energy is considered, and both mountain and valley creases are regarded as elastic hinges, whose elastic potential energy is only related to the origami material, the thickness and the folding angle, as shown in Figure 15 (b).

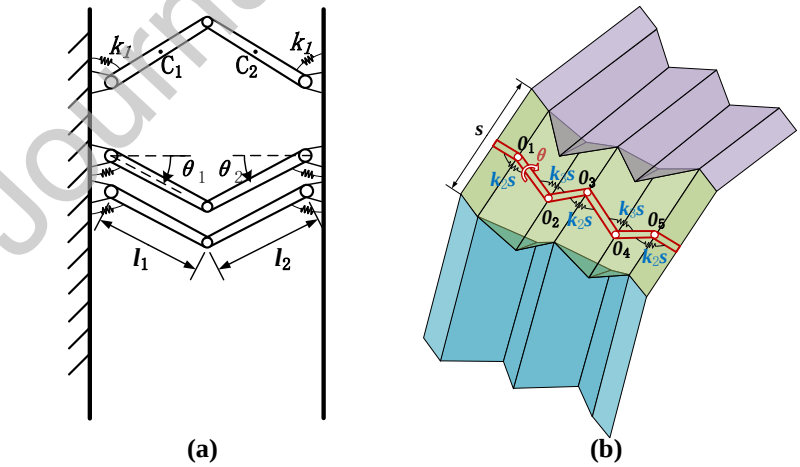

(a) (b)

Figure 15. The equivalent simplified diagram of the spanwise morphing wing unit: (a) the skeleton mechanism; (b) the origami skin.

It is assumed that one of the wing ribs is fixed, and the mountain crease vertices O_1, O_3 and O_5 , and the valley crease vertices O_2 and O_4 only move in the horizontal direction. The mounting angles of the rotating rods are different to achieve additional constraints,

so the dynamic system has only one degree of freedom along the spanwise. The total kinetic energy can be expressed as

$$T = T_1 + 3T_2 \quad (8)$$

where T_1 is the translational kinetic energy of the moving rib and T_2 is the kinetic energy of a pair of rotating rods, which can be described as

$$T_1 = \frac{1}{2} m_1 \dot{x}^2 \quad (9)$$

$$T_2 = \frac{1}{2} m_{C_1} \dot{x}_{C_1}^2 + \frac{1}{2} J_{C_1} \dot{\theta}_1^2 + \frac{1}{2} m_{C_2} \dot{x}_{C_2}^2 + \frac{1}{2} J_{C_2} \dot{\theta}_2^2 \quad (10)$$

where x is the horizontal displacement of the moving rib, m_1 is the mass of the moving rib, m_{C_1} and m_{C_2} are the mass of two adjacent rotating rods, $\dot{x}_{C_1}$ and $\dot{x}_{C_2}$ are their translational velocity, J_{C_1} and J_{C_2} are their moment of inertia, and $\dot{\theta}_1, \dot{\theta}_2$ are their angular velocity. Geometrically, the above parameters can be defined as

$$\dot{x} = -2l \sin\theta \cdot \dot{\theta} \quad (11)$$

$$\dot{x}_{C_1} = \frac{l_1}{2} \cdot \dot{\theta}_1 \quad (12)$$

$$\dot{x}_{C_2} = \frac{l_2}{2} \sqrt{1 + 8\sin^2\theta} \cdot \dot{\theta}_2 \quad (13)$$

$$J_{C_1} = \frac{1}{12} m_{C_1} l_1^2 \quad (14)$$

$$J_{C_2} = \frac{1}{12} m_{C_2} l_2^2 \quad (15)$$

where $l = l_1 = l_2$ are the length of the rotating rods, and $\theta = \theta_1 = \theta_2$ are the angle between the rotating rods and the horizontal line. Besides, $m_{C_1} = m_{C_2} = m_2$.

By substituting Eqs. (9-15) into Eq. (8), the kinetic energy of the spanwise morphing unit can be obtained as

$$T = [(2m_1 + 3m_2)\sin^2\theta + m_2] \cdot l^2 \dot{\theta}^2 \quad (16)$$

Besides, the total potential energy can be expressed as

$$V = 6V_1 + 3V_2 + 2V_3 \quad (17)$$

where V_1, V_2 and V_3 are the elastic potential energy of one torsion spring, one mountain crease and one valley crease.

The torsional stiffness of the torsional spring is defined as

$$k_1 = \frac{E_1 d^4}{64 D_m N} \quad (18)$$

where E_1 is the torsion spring's Young's modulus of a, d is the spring's wire diameter, D_m is the spring's middle diameter, and N is the number of coils.

Then V_1, V_2 and V_3 can be described as

$$V_1 = \frac{1}{2} k_1 \Delta\theta_1^2 \quad (19)$$

$$V_2 = \frac{1}{2} k_2 s \Delta\theta_2^2 \quad (20)$$

$$V_3 = \frac{1}{2} k_3 s \Delta\theta_3^2 \quad (21)$$

where $\Delta\theta_1$ is the angle that the spring rotates from its equilibrium position, $\Delta\theta_2$ and $\Delta\theta_3$ are the angles that the mountain and valley creases rotate from their equilibrium positions, and k is the stiffness per unit length of crease.

It is assumed that the potential energy of the system is zero when the angle between torque arms of the torsion spring is 90°, then the geometric relations can be calculated as

$$\Delta\theta_1 = \Delta\theta_2 = \Delta\theta_3 = \theta \quad (22)$$

By substituting Eqs. (18-22) into Eq. (17), the potential energy of the spanwise morphing unit can be obtained as

$$V = (3k_1 + 7ks)\theta^2 \quad (23)$$

Therefore, the Lagrange function can be described as

$$L = [(2m_1 + 3m_2)\sin^2\theta + m_2] \cdot l^2\dot{\theta}^2 - 3k_1\theta^2 - 7ks\theta^2 \quad (24)$$

According to the second kind of Lagrange equation

$$\frac{d}{dt}\left(\frac{\partial L}{\partial \dot{\theta}}\right) - \frac{\partial L}{\partial \theta} = 0 \quad (25)$$

The kinematic differential equation of the system can be calculated as

$$\ddot{\theta} = \frac{(6k_1+14ks)\cdot\theta+(2m_1+3m_2)\cdot l^2 \sin 2\theta\cdot\dot{\theta}^2}{2l^2[(2m_1+3m_2)\sin^2\theta+m_2]} \tag{26}$$

Substituting the specific geometry of the system into Eq. (26), the $\theta - t$ curve can be drawn, as shown in Figure 16 (a). The $\theta - t$ curve displays how the generalized coordinate (θ) changes over time (t) when the spanwise morphing unit expands from fully folded, and the initial value of θ is 90°. Because of the self-locking structure, the system can be locked when the unit is fully spread, and no rebound or large vibration occurs. At this time, θ is exactly 0°. In other words, when $\theta = 0^\circ$ for the first time, the system achieves self-locking and no further periodic motion occurs. Therefore, only part of the curve segment before $\theta = 0^\circ$ for the first time needs to be considered, as shown in Figure 16 (b).

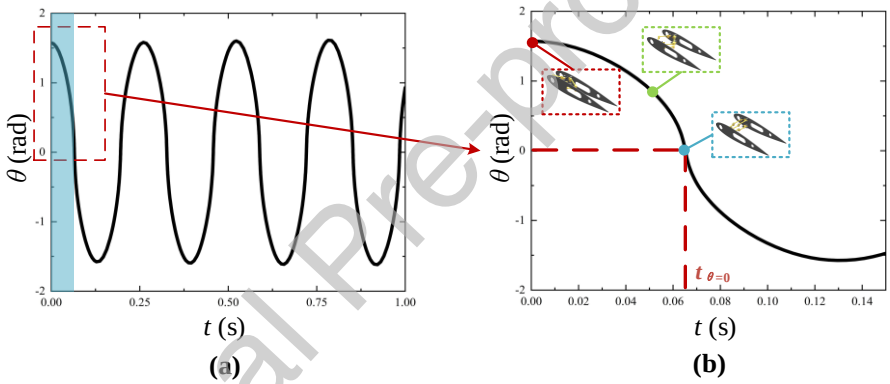

Figure 16. The generalized coordinate (θ) changes over time (t): (a) the whole curve; (b) the first part of the curve.

$t = t_{\theta=0}$ represents the time required for one unit to get fully expanded, and the slope of the curve represents the generalized velocity of the unit at this moment. Thus, the total kinetic energy is obtained, which can be compared with the minimum energy absorption obtained in Section 2.3 to check the reliability of the lockable structure.

1.1. Dynamic analysis of multiple units

According to the dynamic analysis of a single spanwise morphing unit, one unit is simplified into a single spring-slider system, as shown in Figure 17, where k is the equivalent stiffness and m is the equivalent mass of the system.

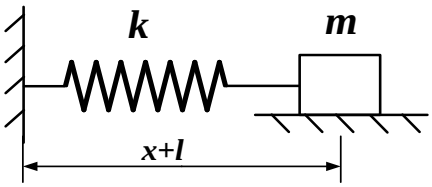

Figure 17. The single spring-slider system.

Similarly, the kinematic differential equation of the system can be obtained by the second Lagrange equation, which can be described as

$$\ddot{x} = -\frac{k}{m}x \tag{27}$$

where x is the displacement from the slider's equilibrium position, l is the spring's original length.

The $x-t$ curve can be drawn in Figure 18, and it can be obtained that $t_{x=0} = 0.1570$s, where $t_{x=0}$ is the time that the spring-slider system takes to reach its equilibrium position for the first time.

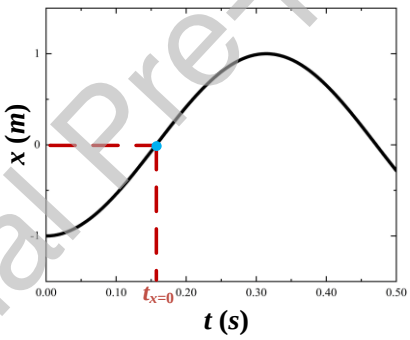

Figure 18. The displacement (x) changes over time (t).

Analogously, when two, three and more spanwise morphing wing units are connected in series, the models can be simplified into a two spring-slider system as shown in Figure 19 (a), a three spring-slider system as shown in Figure 19 (b), and so on. For an n spring-slider system, the number of degrees of freedom is n. Each spring obtains zero potential energy when it is at the equilibrium position, and the generalized coordinates are $x_1, x_2 \cdots x_n$, which indicate the displacement from each equilibrium position. Then the total kinetic energy and potential energy can be expressed as

$$T = \frac{1}{2}m\dot{x}_1^2 + \frac{1}{2}m(\dot{x}_1 + \dot{x}_2)^2 + \cdots + \frac{1}{2}m(\dot{x}_1 + \dot{x}_2 + \cdots + \dot{x}_n)^2 \tag{28}$$

$$V = \frac{1}{2}kx_1^2 + \frac{1}{2}kx_2^2 + \cdots + \frac{1}{2}kx_n^2 \tag{29}$$

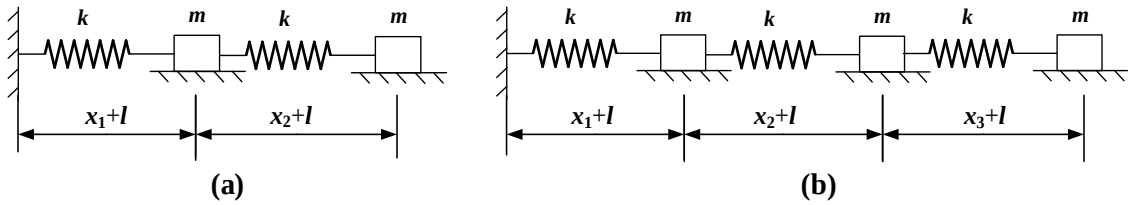

Figure 19. Multiple units: (a) double spring-slider system; (b) three spring-slider system.

Taking two spring-slider and three spring-slider as examples, the Lagrange equation can be expressed respectively as Eq. (30) and Eq. (31). Then the kinematic differential equations are calculated as Eq. (32) and Eq. (33), thus the $t_{x=0}$ of each unit is obtained, as shown in Figure 20 and Figure 21. For the two spring-slider system, the $t_{x=0}$ of each unit are 0.1916s and 0.2640s along the direction from the free end to the fixed end. And for the three spring-slider system, the $t_{x=0}$ of each unit are 0.1916s, 0.3029s and 0.3960s along the direction from the free end to the fixed end.

$$L_1 = \frac{1}{2}m\dot{x}_1^2 + \frac{1}{2}m(\dot{x}_1 + \dot{x}_2)^2 - \frac{1}{2}kx_1^2 - \frac{1}{2}kx_2^2 \tag{30}$$

$$L_2 = \frac{1}{2}m\dot{x}_1^2 + \frac{1}{2}m(\dot{x}_{1+}\dot{x}_2)^2 + \frac{1}{2}m(\dot{x}_1 + \dot{x}_2 + \dot{x}_3)^2 - \frac{1}{2}kx_1^2 - \frac{1}{2}kx_2^2 - \frac{1}{2}kx_3^2 \tag{31}$$

$$\ddot{x}_1 = \frac{kx_2 - kx_1}{m}, \ddot{x}_2 = \frac{kx_1 - 2kx_2}{m} \tag{32}$$

$$\ddot{x}_1 = \frac{kx_2 - kx_1}{m}, \ddot{x}_2 = \frac{kx_1 - 2kx_2 + kx_3}{m}, \ddot{x}_3 = \frac{kx_2 - 2kx_3}{m} \tag{33}$$

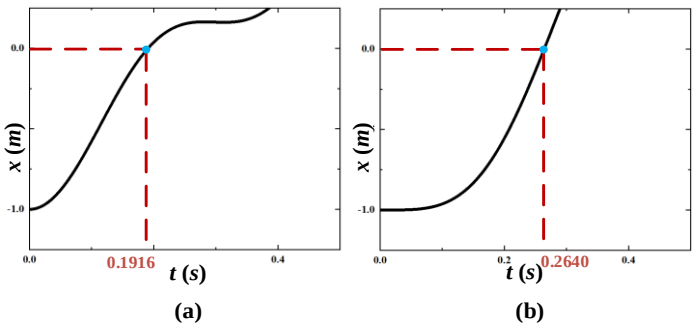

Figure 20. The generalized coordinate (x_i) changes over time (t) in the two spring-slider system: (a) the unit near the free end; (b) the unit near the fixed end.

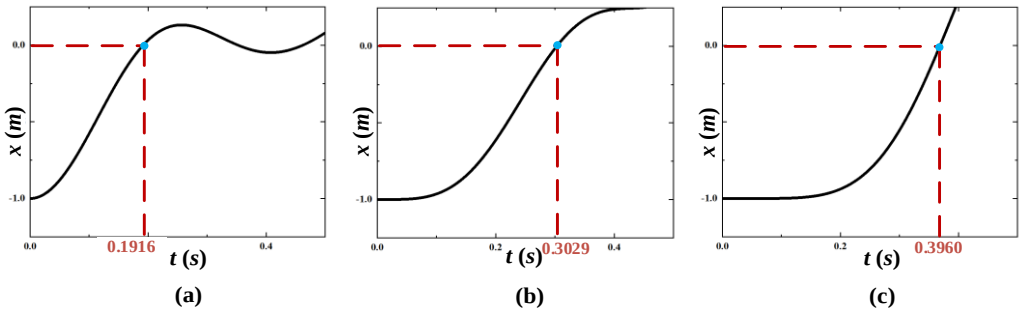

Figure 21. The generalized coordinate (x_i) changes over time (t) in the three spring-slider system: (a) the unit near the free end; (b) the middle unit; (c) the unit near the fixed end.

By analogy, the four spring-slider system and the five spring-slider system are calculated as well, and the results are shown in Figure 22.

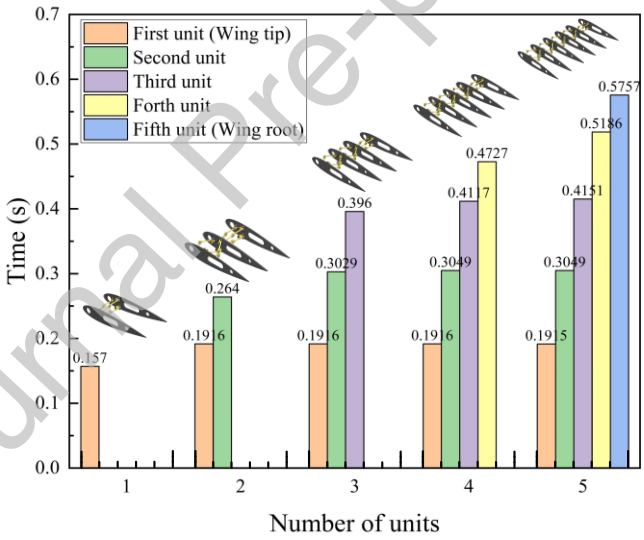

Figure 22. The $t_{x=0}$ of each unit for different numbers of units.

As the spanwise morphing wing consisting of multiple modular units, the spring-slider system is a simplification of one modular unit for dynamic analysis. The spring representing the wing's torsional spring and the slider representing the moving wing rib and rotating rods. The spring slider unit near the fixed end and free end represents the spanwise morphing unit near the wing root and the wing tip, respectively. Therefore, from Figure 22 it can be obtained that the unit near the wing tip has the minimum fully deployed time, which increases from the wing tip to the wing root for each unit. In other words, the spanwise morphing unit closest to the wing tip has the shortest time to get

fully expanded, and the time to get fully expanded increases unit-by-unit along the direction from the wing tip to the wing root. Furthermore, when the number of units is $n\ (n > 2), t_{x=0}$ of the $n-2$ units near the wing tip are the same as $t_{x=0}$ of the corresponding units when the number of units is $n-1$.

4. FSI analysis of the spanwise morphing wing unit

The design of the spanwise morphing wing needs to consider the deformation and the stress distribution under aerodynamic loads. This article uses a one-way fluid-structure coupling interaction (FSI) to analyse the effect on the skeleton mechanism and the origami skin under aerodynamic loads. Ansys Workbench is used to establish the FSI-simulated platform. The fluid simulation is calculated by Fluent, and the morphing wing's structural simulation is calculated by Static Structural Analysis.

4.1. Finite element model

The finite element model (FEM) model of the morphing wing unit is established, as shown in Figure 23. The skeleton mechanism uses a Sarrus linkage structure to support the origami skin and bear the aerodynamic load. The rotating rods and wing ribs are connected by rotating joints, and the bonded contact is set between the origami skin and the wing rib. Then the skeleton mechanism and origami skin are meshed in Static Structural Analysis.

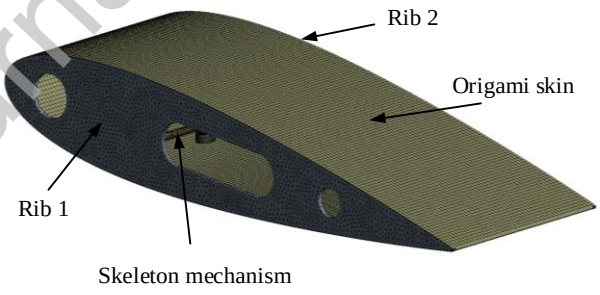

Figure 23. The spanwise morphing wing's FEM model.

The material properties of different structures are listed in Table 3. The skeleton's material is polylactic acid (PLA), the skin material is polyethylene terephthalate (PET) with 0.2mm thickness, and the bearing and axle material is stainless steel.

Table 3. Material and material properties of different structures.

Structure	Material	Density (g/cm^3)	Young's modulus (MPa)	Poisson's Ratio
Wing rib	PLA	1.17	2636	0.28
Rotating rod	PLA	1.17	2636	0.28
Bearing	Steel	7.85	2.1×10^5	0.3
Axle	Steel	7.85	2.1×10^5	0.3
Skin	PET	0.90	400	0.23

The fluid-structure coupling simulation interface is created on the origami skin, and the FEM model is solved in Static Structural. One wing rib is fixed, and the aerodynamic load is applied to the origami skin. The skin's and skeleton's stress and deformation under aerodynamic loads are obtained under the solution time for 2s.

4.2. CFD fluid model

The fluid model of the FSI analysis is created based on the FEM model, as shown in Figure 24. It is assumed that the pressure outlet boundary condition is located at the vertical edge of the computational domain and the velocity inlet boundary condition is located at the remaining outer edge of the computational domain. The sides of the fluid domain are set as symmetrical planes to reduce unnecessary calculation errors.

A C-mesh fluid model is used to perform the simulations, which extends $7.5c$ from the semi-circular edge and $15c$ from the vertical edge, where $c = 144$mm is the rib's chord length. The width of the fluid domain is 144mm, which is the same as the rib spacing of the morphing wing. The hexagonal grid is used for fluid meshing, and a rectangular area surrounding the airfoil is encrypted. The total element number is 1.53 million, as shown in Figure 25.

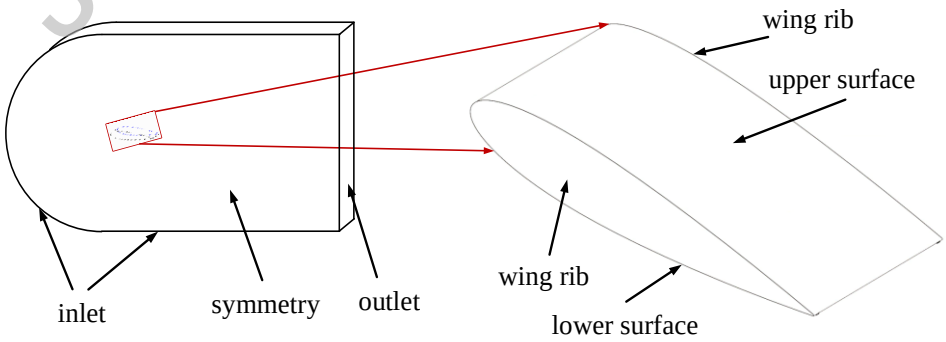

Figure 24. The fluid domain and its naming.

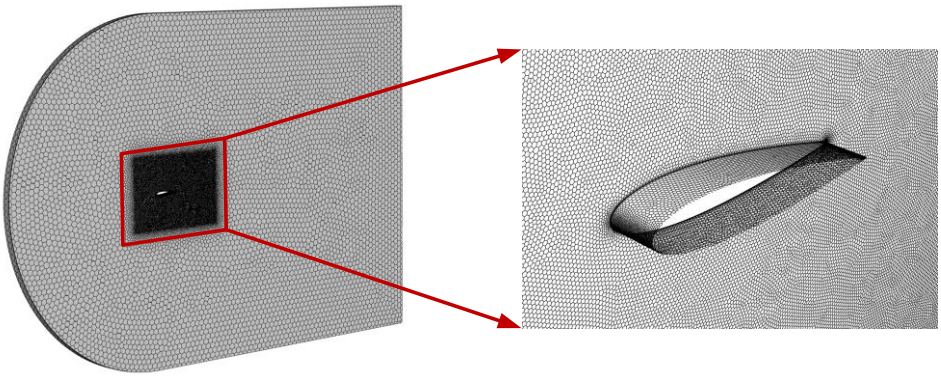

Figure 25. CFD mesh of the fluid domain with the spanwise morphing wing.

The fluid model is simulated in Fluent, and the fluid computational parameters are set as follows: the gas density $\rho = 1.15\text{kg/m}^3$, the flight speed Ma = 0.059, Reynolds number $Re = 6 \times 10^6$, angle of attack $AOA = 6°$, reference temperature $T = 320\text{K}$. The k-w SST turbulence model is set as the turbulence model, and Sutherland is select as the viscosity. The aerodynamic load influences the morphing wing primarily through the stress and deformation distribution of the morphing wing unit.

4.3. Discussion of the FSI analysis

Figure 26 (a) shows the static pressure distribution near the airfoil, calculated by CFD fluid simulation. To directly express the static pressure distribution along the airfoil surface, the x-y curve of the static pressure is obtained, as shown in Figure 26 (b). The minimum pressure is located at the upper leading edge, and the maximum pressure is located at the lower leading edge surface. Most upper and lower surfaces are negative pressure areas. Only areas near the trailing edge surface and those near the lower leading edge surface show positive pressure.

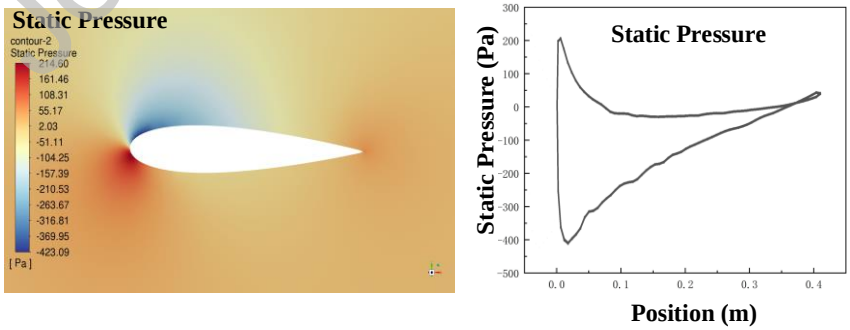

(a) **(b)**

Figure 26. The distribution of static pressure: (a) near the airfoil surface; (b) along the airfoil surface.

The aerodynamic load is applied to the origami skin surface, and the structural deformation distribution and stress distribution are shown in Figure 27. It is observed that the deformation of the rotating rods is minimal, indicating that the rotating rods can provide sufficient stiffness to support the aerodynamic loads. On the other hand, the maximum stress is 10.356MPa, which is less than the yield strength of the material chosen in this article (PLA 60 MPa and stainless steel 260 MPa), proving that the skeleton structure meets the strength requirements. Moreover, the maximum stress is located at the joint between the wing rib and the rotating rod, which provides an essential reference for design improvement.

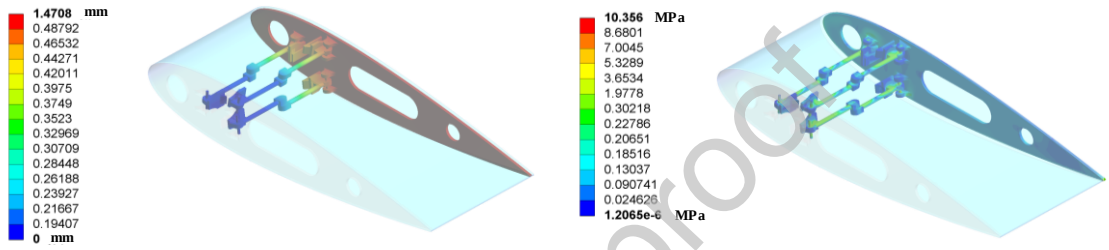

(a) **(b)**

Figure 27. Structural deformation distribution and stress distribution: (a) deformation; (b) stress.

The out-of-plane deformation and stress distribution of origami skin under aerodynamic load are shown in Figure 28. The maximum deformation is mainly located at the upper surface, which is sucked out of the skin surface due to the negative pressure calculated by CFD simulation. What's more, there is a region with positive pressure on the upper trailing edge surface, which causes this area of skin to be sucked into the skin surface. The origami skin's maximum stress is below the PET material's yield strength (50 MPa), demonstrating that the skin will not be damaged under the aerodynamic load. Besides, the criteria for out-of-plane deformation shows that the maximum deformation of the wing skin is supposed to be less than 0.5% of the chord length under the aerodynamic pressure, so the aerodynamic-carrying capacity of the origami skin will be proofread. The maximum deformation of the skin is 1.47 mm which is lower than 0.5% of the chord length ($400\text{mm} \times 0.5\% = 2\text{mm}$), indicating that the skin meets the demand for deformation capacity.

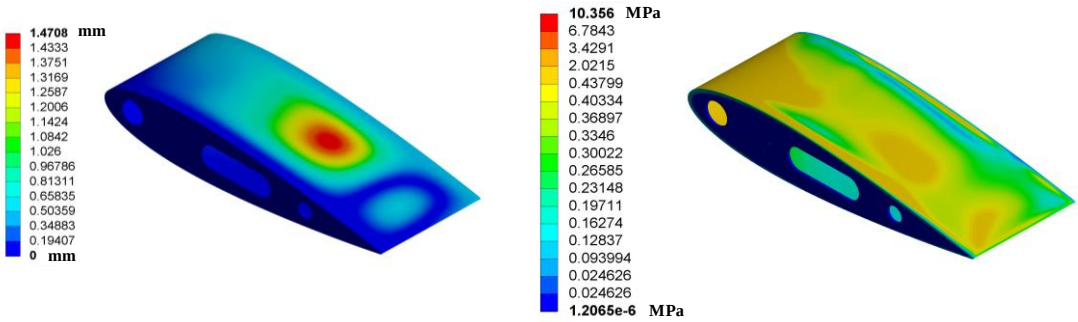

(a) **(b)**

Figure 28. The skin's deformation distribution and stress distribution: (a) deformation; (b) stress.

5. Flight test

A flight test is carried out to verify the performances of the spanwise morphing UAV after expansion and whether the various performance indexes of the spanwise morphing wing meet the design requirements.

Ground run test, take-off test, elliptical flight test and overload flight test are carried out respectively, as shown in Figure 29 (a)-(d). The flight test on the elliptical route means that under the cruise throttle state, the flight roll angle is maintained at 30°. A significant turning radius is flown in the air, and the flight attitude is observed. The flight data is recorded to check the flight performance of the UAV and determine whether there are defects in structural design. The overload flight test is used to verify whether the structural strength of the spanwise morphing wing satisfies the flight load requirements under the condition of 2.5g maximum forward overload and 1g maximum reverse overload.

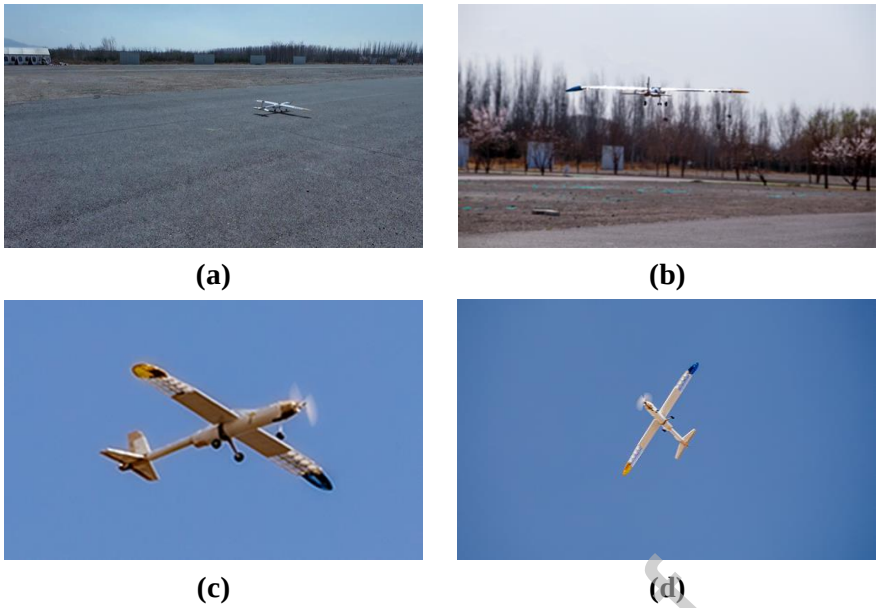

(a) (b)

(c) (d)

Figure 29. Photos for flight performance test taken from the ground: (a) ground run test; (b) take-off test; (c) elliptical flight test; (d) overload flight test.

The results show that a mutational wind or overload condition brings more deflection to the spanwise morphing wing structure, as shown in Figure 30. However, the flight attitude and stability of the UAV are not significantly affected, and it's found that there is no invalidation or damage to the wing structure through the inspection after flight tests. Therefore, the structural strength satisfies the flight load requirements and the flight test verified the feasibility and reliability of the span morphing wing design.

(a) (b)

Figure 30. Photos for flight performance test taken from the on-board camera: (a) large deflection of the wing structure; (b) small deflection of the wing structure.

6. Conclusions

A new concept for the spanwise morphing wing with modular units has been presented, which can solve the transportation problem of the large-size Mars exploration vehicle. The cross-section shape of the foldable truss along the wing chord is discussed to achieve

higher structural stiffness as well as lighter structural mass. A lockable snap-fit structure is designed to provide stiffness and stability after the expansion of the morphing wing, and the main parameters that affect the property of the lockable structure are analysed. The Miura-Waterbomb origami skin is proposed, and the creases' parameters and the rigid folding geometry are derived.

The kinematics of the spanwise morphing wing unit and the theoretical models of the morphing wing with different numbers of units are conducted according to the second Lagrange equation. The result indicates that the unit near the wing tip has the minimum time to get full expansion, and this time increases from the wing tip to the wing root.

The FSI analysis is carried out to obtain the deformation and stress distribution of the morphing wing mechanism. The results demonstrate that the structural maximum stress is below the yield strength of the material chosen in this article, and the skin's maximum out-of-plane deformation is less than 0.5% of the wing chord. Therefore, the stiffness of the spanwise morphing wing satisfies the requirement under the aerodynamic load.

At last, the flight test is carried out to verify whether the stiffness of the morphing structure meets the flight load requirements, and the results align with expectations. That is to say, the spanwise morphing mechanism can withstand a certain aerodynamic load without failure or damage.

However, the proposed spanwise morphing wing design still has some limitations, which cannot fully satisfy the requirements for the Mars exploration mission. For example, the morphing mechanism requires a larger airfoil thickness, which produces higher aerodynamic resistance. Besides, due to the limitations of 3D printing materials and modeling processes, the morphing wing structure can be damaged or fail in complex aerodynamic environments, which would be catastrophic for deep space exploration aircraft. Consequently, future research will focus on optimizing the mechanism parameters and enhancing the structural stiffness and strength. While the concept proposed in the paper is relatively simple, they provide an approach to gain insights into morphing wings which can be extended to achieve potential applications for the Mars exploration mission.

Acknowledgments

This project has received funding from National Natural Science Foundation of China (Grant No. 92271104, 12102017) and Beijing Natural Science Foundation (Grant No. 1232014).

References

[1] K.A. Farley, K.H. Williford, K.M. Stack, R. Bhartia, A. Chen, M. de la Torre, K. Hand, Y. Goreva, C.D. Herd, R. Hueso, Mars 2020 mission overview, Space Science Reviews, 216 (2020) 1-41.

[2] E. Karpovich, T. Kombaev, D. Gueraiche, D. Evdokimova, K. Alexandrov, Long-Endurance Mars Exploration Flying Vehicle: A Project Brief, Aerospace, 10 (2023) 965.

[3] N. Dhanji, Comparative Study of Aerial Platforms for Mars Exploration, Journal of the British Interplanetary Society, 68 (2015) 282-296.

[4] B. Balaram, T. Canham, C. Duncan, H.F. Grip, W. Johnson, J. Maki, A. Quon, R. Stern, D. Zhu, Mars helicopter technology demonstrator, 2018 AIAA atmospheric flight mechanics conference, 2018, pp. 0023.

[5] C. Kuhl, Design of a Mars airplane propulsion system for the aerial regional-scale environmental survey (ARES) mission concept, 44th AIAA/ASME/SAE/ASEE Joint Propulsion Conference & Exhibit, 2008, pp. 5246.

[6] Z. Terze, V. Pandža, M. Kasalo, D. Zlatar, Discrete mechanics and optimal control optimization of flapping wing dynamics for Mars exploration, Aerospace science and technology, 106 (2020) 106131.

[7] A. Bouskela, A. Kling, T. Schuler, S. Shkarayev, H. Kalita, J. Thangavelautham, Mars exploration using sailplanes, Aerospace, 9 (2022) 306.

[8] S. Barbarino, O. Bilgen, R.M. Ajaj, M.I. Friswell, D.J. Inman, A review of morphing aircraft, Journal of intelligent material systems and structures, 22 (2011) 823-877.

[9] R.M. Ajaj, M.I. Friswell, E. I Saavedra Flores, A. Keane, A.T. Isikveren, G. Allegri, S. Adhikari, An integrated conceptual design study using span morphing technology, Journal of intelligent material systems and structures, 25 (2014) 989-1008.

[10] T.A. Weisshaar, Morphing aircraft technology-new shapes for aircraft design, Multifunctional Structures/Integration of Sensors and Antennas, (2006) O1-1.

[11] J. Zhang, C. Bisagni, Buckling-driven mechanisms for twisting control in adaptive composite wings, Aerospace Science and Technology, 118 (2021) 107006.

[12] M.S. Parancheerivilakkathil, A compliant polymorphing wing for small UAVs, Chinese Journal of Aeronautics, 33 (2020) 2575-2588.

[13] M. Love, S. Zink, R. Stroud, D. Bye, C. Chase, Impact of actuation concepts on morphing aircraft structures, 45th AIAA/ASME/ASCE/AHS/ASC Structures, Structural Dynamics & Materials Conference, 2004, pp. 1724.

[14] D. Cadogan, W. Graham, T. Smith, Inflatable and rigidizable wings for unmanned aerial vehicles, 2nd AIAA" Unmanned Unlimited" Conf. and Workshop & Exhibit, 2003, pp. 6630.

[15] J. Rowe, S. Smith, A. Simpson, J. Jacob, S. Scarborough, Development of a finite element model of warping inflatable wings, 47th AIAA/ASME/ASCE/AHS/ASC Structures, Structural Dynamics, and Materials Conference 14th AIAA/ASME/AHS Adaptive Structures Conference 7th, 2006, pp. 1697.

[16] J. Blondeau, D. Pines, Pneumatic morphing aspect ratio wing, 45th AIAA/ASME/ASCE/AHS/ASC Structures, Structural Dynamics & Materials Conference, 2004, pp. 1808.

[17] J. Vale, A. Leite, F. Lau, A. Suleman, Design and development of strategies and structures for wing morphing, The Applied Vehicle Technology Panel Symposium (AVT-168), Évora, Portugal, 2009, pp. 20-23.

[18] J.B. Samuel, D. Pines, Design and testing of a pneumatic telescopic wing for unmanned aerial vehicles, Journal of Aircraft, 44 (2007) 1088-1099.

[19] R.M. Ajaj, G.K. Jankee, The Transformer aircraft: A multimission unmanned aerial vehicle capable of symmetric and asymmetric span morphing, Aerospace Science and Technology, 76 (2018) 512-522.

[20] M. Kölbl, P. Ermanni, Structural design and analysis of an anisotropic, bi-axially morphing skin concept, Aerospace Science and Technology, 120 (2022) 107292.

[21] R. Ajaj, E.S. Flores, M. Friswell, G. Allegri, B. Woods, A. Isikveren, W. Dettmer, The Zigzag wingbox for a span morphing wing, Aerospace Science and Technology, 28 (2013) 364-375.

[22] M.P. Snyder, B. Sanders, F.E. Eastep, G.J. Frank, Vibration and flutter characteristics of a folding wing, Journal of Aircraft, 46 (2009) 791-799.

[23] J. Zhang, A.D. Shaw, C. Wang, H. Gu, M. Amoozgar, M.I. Friswell, Resonant passive energy balancing for a morphing helicopter blade, Aerospace Science and Technology, 128 (2022) 107786.

[24] J. Zhang, C. Wang, A.D. Shaw, M. Amoozgar, M.I. Friswell, Passive energy balancing design for a linear actuated morphing wingtip structure, Aerospace Science and Technology, 107 (2020) 106279.

[25] M.K.H. Pulok, U.K. Chakravarty, Aerodynamic and vibration analysis of the morphing wings of a hypersonic vehicle, ASME International Mechanical Engineering Congress and Exposition, American Society of Mechanical Engineers, 2020, pp. V004T004A013.

[26] H. Yang, S. Jiang, Y. Wang, H. Xiao, Design, kinematic and fluid-structure interaction analysis of a morphing wing, Aerospace Science and Technology, 143 (2023) 108721.

[27] P. Gamboa, P. Santos, J. Silva, P. Santos, Flutter analysis of a composite variable-span wing, 4th international conference on integrity, reliability and failure, Funchal, 2013, pp. 23-27.

[28] J. S. Bae, T.M. Seigler, D.J. Inman, Aerodynamic and static aeroelastic characteristics of a variable-span morphing wing, Journal of aircraft, 42 (2005) 528-534.

[29] D. Neal, M. Good, C. Johnston, H. Robertshaw, W. Mason, D. Inman, Design and wind-tunnel analysis of a fully adaptive aircraft configuration, 45th AIAA/ASME/ASCE/AHS/ASC Structures, Structural Dynamics & Materials Conference, 2004, pp. 1727.

[30] J. Zhang, A.D. Shaw, C. Wang, H. Gu, M. Amoozgar, M.I. Friswell, B.K. Woods, Aeroelastic model and analysis of an active camber morphing wing, Aerospace Science and Technology, 111 (2021) 106534.

[31] T. W. Liu, J.-B. Bai, N. Fantuzzi, G. Y. Bu, D. Li, Multi-objective optimisation designs for thin-walled deployable composite hinges using surrogate models and Genetic Algorithms, Composite Structures, 280 (2022) 114757.

[32] F. Yang, Z. You, Y. Chen, Foldable hexagonal structures based on the threefold-symmetric Bricard linkage, Journal of Mechanisms and Robotics, 12 (2020) 011012.

[33] J. Cui, S. Yan, J. Hu, Z. Chu, A metric to design spring stiffness of underactuated fingers for stable grasp, Robotics and Autonomous Systems, 102 (2018) 1-12.

[34] M. Amoozgar, A. Shaw, J. Zhang, C. Wang, M. Friswell, Lag-twist coupling sensitivity and design for a composite blade cross-section with D-spar, Aerospace Science and Technology, 91 (2019) 539-547.

[35] B. Jenett, S. Calisch, D. Cellucci, N. Cramer, N. Gershenfeld, S. Swei, K.C. Cheung, Digital morphing wing: active wing shaping concept using composite lattice-based cellular structures, Soft robotics, 4 (2017) 33-48.

[36] N.M. Mahid, B.K.S. Woods, Initial exploration of a compliance-based morphing fairing concept for hinged aerodynamic surfaces, Aerospace Science and Technology, 136 (2023) 108244.

[37] Q. Wang, Y. Chen, H. Tang, Mechanism design for aircraft morphing wing[C]//53rd AIAA/ASME/ASCE/AHS/ASC Structures, Structural Dynamics and Materials Conference 20th AIAA/ASME/AHS Adaptive Structures Conference 14th AIAA. 2012: 1608.

[38] K. Fujita, R. Luong, H. Nagai, K. Asai, Conceptual design of Mars airplane. Transactions of the Japan Society for Aeronautical and Space Sciences, Aerospace Technology Japan, 10.ists28(2012), Te_5-Te_10.

Declaration of interests

☒ The authors declare that they have no known competing financial interests or personal relationships that could have appeared to influence the work reported in this paper.

☐ The authors declare the following financial interests/personal relationships which may be considered as potential competing interests: